

# Quantum phase transitions far from equilibrium in short-range transverse field Ising models

Ceren B. Dağ\* and Kai Sun

Department of Physics, University of Michigan, Ann Arbor, Michigan 48109, USA

(Dated: November 19, 2021)

Dynamical phase transitions (DPTs) are generally defined under two different but related categories: DPT-I where the equilibrium value, or long-time average, of the order parameter as a function of the control parameter demonstrates a phase boundary; DPT-II where the Loschmidt return rate shows a cusp singularity in real-time dynamics. Quenched from polarized states, one-point observables have featureless steady state regimes for short-range transverse field Ising models (TFIM), which prevents them from exhibiting DPT-I, unlike long-range TFIM. In this Letter, we incorporate Lieb-Robinson bounds into the definition of DPT by choosing appropriate temporal cutoffs and show that in the lightcone, a quantum phase transition (QPT) *far from equilibrium* could emerge with an associated scaling law at the vicinity of the transition. More specifically, the observable at the cutoff could exhibit order parameterlike behavior in analogy to equilibrium quantum criticality, however with certain important differences that we discuss in detail. The scaling of the dynamical order parameter at the vicinity is determined via the decay rate of the observable in time, hence rendering the QPT a truly nonequilibrium phase transition. We apply the procedure to both integrable and nonintegrable short-range TFIM and elaborate on how the QPT signature changes with integrability.

*Introduction.* Criticality, defined under Landau paradigm [1], is one of the milestones in our understanding of matter, providing us a framework to classify microscopically diverse phenomena in a handful of universality classes with their associated critical exponents [2, 3]. Its dynamical counterpart, dynamical criticality, studies both the imprints of equilibrium criticality on dynamics [4–14] and genuine non-equilibrium criticality that does not necessarily originate from an equilibrium transition [11, 12, 15–21]. Dynamical phase transitions (DPT) could in general be classified via two different but related definitions [11, 19, 22]: DPT-I and DPT-II. DPT-I is defined based on the time evolution of an (equilibrium) order parameter (OP) quenched from a state that is not an eigenstate of the evolution Hamiltonian [11]. In the ordered phase where the control parameter originates from the equilibrium transition, a prethermal regime appears with either equilibration or oscillatory saturation. Hence the long-time average of the signal could act like a dynamical OP, demonstrating a phase boundary. DPT-II concerns with cusp singularity appearing at critical times of the return rate that is based on Loschmidt echo and is linked to equilibrium phase transitions [9–11, 19, 22]. Although DPT-I is well-defined for long-range TFIM with one-point observables [18, 19], there is no persistent dynamic order for short-range Hamiltonians, simply because the steady state regime of one-point observables, and likewise two-time correlators (TTC), for such systems is featureless [23–25]. Recently higher order correlators are demonstrated to host a DPT-I for short-range TFIM [12, 21]. However since one-point observables are both computationally and experimentally more accessible, in particular with polarized initial states [20, 26–30], it is still an interesting and significant direction to explore

the potential of these observables in supporting a QPT far from equilibrium.

We first note that the conventional temporal cutoff often utilized in DPT-I studies, namely  $t \sim N$  where the interval of time-averaging is proportional to the system size does not work for one-point observables in short-range models, because of two reasons: (i) As already mentioned before, these observables are featureless in their steady state regime, and (ii) there are more significant timescales for these observables that require the incorporation of Lieb-Robinson bounds [24, 31, 32] into the definition of DPT for short-range TFIM. Hence this timescale is based on the maximum propagation velocity of excitations that can be hosted in the system. Motivated by this timescale, we study both parametric and fixed temporal cutoffs where  $t \sim v_q^{-1}$  and  $t \sim \text{constant}$ , respectively as long as the dynamics remain in the lightcone. Bounding the dynamics by lightcone, additionally makes the results system size independent, significantly reducing the finite-size effects.

The featureless steady-state for one-point observables origins from the fact that these observables decay exponentially in time as both analytically and numerically studied in the integrable TFIM [23–25, 33–35]. In fact exponential decay is also shown to exist in the XXZ model for one-point observables [36]. By studying how decay rate changes with the control parameter, we show that the scaling of dynamical OP can be obtained at the vicinity of the transition. Similar to the observation in the XXZ model [36], the decay rate has a sharp feature at the transition depending on the integrability of the model. We determine the dynamic transition point as  $h_c = 0.9999 \pm 0.0001$  for integrable TFIM with an associated scaling exponent  $\text{OP} \sim h^\beta$  of  $\beta = 1$ , which is linear in the control parameter  $h$ . Breaking integrability

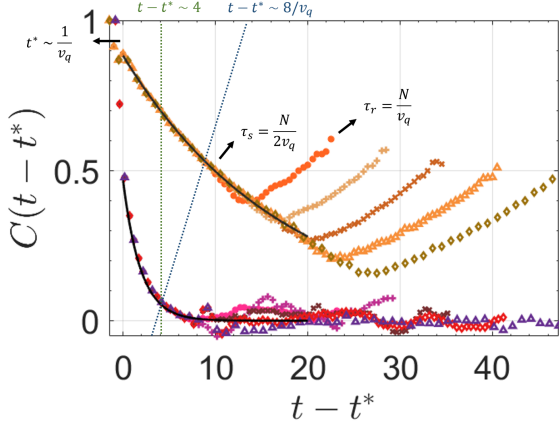


FIG. 1.  $C(t)$  for  $h/J = 0.5$  upper curves with orange tones and  $h/J = 0.9$  lower curves with red tones. Each set of curves have system sizes between  $N = 24$  (dots) and  $N = 48$  (diamonds) denoted by different markers.  $\tau_s$  and  $\tau_r$  are separation and revival timescales (see text). x-axis is shifted with  $t^*$ , the reference time where the exponential decay starts. Green- and blue-dotted lines show two different temporal cutoffs applied in the study, fixed and parametric, respectively.

smooths out and shifts the signature of phase boundary from its equilibrium counterpart. We determine the transition point as  $h_c = 2.278 \pm 0.001$  with  $\beta \sim 2$  for our nonintegrable TFIM.

*Temporal cutoffs.* A TTC  $C(t) = \langle \psi_0 | \sigma_r^z(t) \sigma_r^z | \psi_0 \rangle$  where  $|\psi_0\rangle = |\uparrow\uparrow \dots \uparrow\rangle$  is a polarized state, could be reduced to one-point observable  $C(t) = \langle \psi_0 | \sigma_r^z(t) | \psi_0 \rangle$  where  $\sigma_r^z$  is a local spin operator of a bulk spin. Let us introduce TFIM with both nearest-neighbor (NN) and next-nearest-neighbor (NNN) couplings,

$$H = -J \sum_r \sigma_r^z \sigma_{r+1}^z - \Delta \sum_r \sigma_r^z \sigma_{r+2}^z + h \sum_r \sigma_r^x, \quad (1)$$

with open boundaries and where  $\sigma_r^\alpha$  are spin- $\frac{1}{2}$  Pauli spin matrices. TFIM preserves its gapped long range Ising ground state even when the interactions (or non-integrability)  $\Delta$  are introduced, although the transition boundary shifts to favor order as  $\Delta$  increases.

It is well-known that two-point correlators in space show lightcone effect [34, 37–39] with a well-defined hierarchy of timescales for asymptotically far away spins [24] based on the quasi-particle velocity  $v_q$ . We observe that  $C(t)$ , our one-point observable, can also exhibit lightcone effect, however quite different than how two-point correlators do. Fig. 1 shows the dynamics for  $h/J = 0.5$  (orange tones) and  $h/J = 0.9$  (red tones) for system sizes ranging between  $N = 24$  (dots) and  $N = 48$  (diamonds). In the lightcone, data for different system sizes collapse on each other while each separation point is roughly marked by  $\tau_s = N/2v_q$  where  $v_q$  is the maximum quasi-particle velocity  $v_q = \max|d\epsilon(h, k)/dk| = 2J\min(h, 1)$

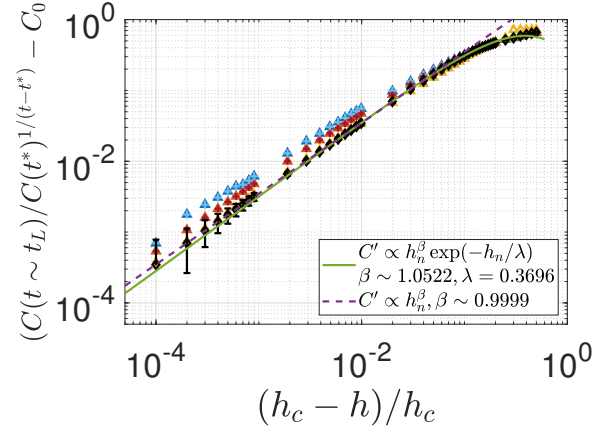


FIG. 2. The scaling at the vicinity of the transition for integrable TFIM with respect to reduced control parameter  $h_n$ . y-axis is rescaled correctly to obtain the scaling (see text). The blue, red and yellow data are either fixed temporal cutoffs at times  $t = 5.5, 4, 2.5$  (crosses) or parametric  $t = \alpha v_q^{-1}$  with  $\alpha = 11, 8, 5$  (triangles). Black-diamond line is data originated from the decay data analysis (see text). Purple-dashed line shows a power-law scaling with exponent  $\beta = 1$  at the vicinity of the transition while the green-solid line is power-law scaling with exponential cutoff to determine the vicinity of the transition,  $h_n \ll \Lambda = 0.37$ .

[3].  $\tau_s$  is the time for the excitations caused by the quench to reach the end of the chain, and hence  $\tau_s$  probes the size of the chain. When the chosen bulk spin is not at the middle of the chain its coefficient changes  $\tau_s = \alpha/v_q$  where  $N/2 \leq \alpha < N$ . Revival timescale is marked by  $\tau_r = N/v_q$ , which is the time for the excitations to reflect back from the boundary to the middle of the chain. The timescale  $t^*$  is the short-distance cutoff of the temporal axis defined by the lattice constant divided by velocity  $t^* \sim v_q^{-1}$ . Here,  $t^*$  ( $\tau_s$ ) serves as the ultraviolet (infrared) cutoff, below (above) which the physics is dominated by non-universal microscopic details (finite-size effects). Thus, we focus on the (intermediate) time range  $t^* < t < \tau_s$ , where data of different system sizes collapse on each other and universal behavior arises as shown in Fig. 1 with an exponential decay [33–35]. We choose the dynamical OP as the corresponding  $C(t \sim t_L)$  where the temporal cutoff is applied at  $t_L$  and study two different cutoffs: (i) fixed  $t \sim \text{constant}$  (green-dotted) and (ii) parametric  $t \sim \alpha v_q^{-1}$  (blue-dotted) where  $\alpha$  is chosen so that the dynamic response remains in the lightcone.

*QPT far from equilibrium.* In DPT-I, one studies steady-state regime where the dynamics becomes independent of the time. Hence where the temporal cutoff  $t \sim N$  is exactly applied is not significant in the construction of the dynamical OP based on DPT-I as long as the temporal cutoff is in steady-state regime. To define a DPT with one-point observables for short-range models, we need to focus on the intermediate time range where

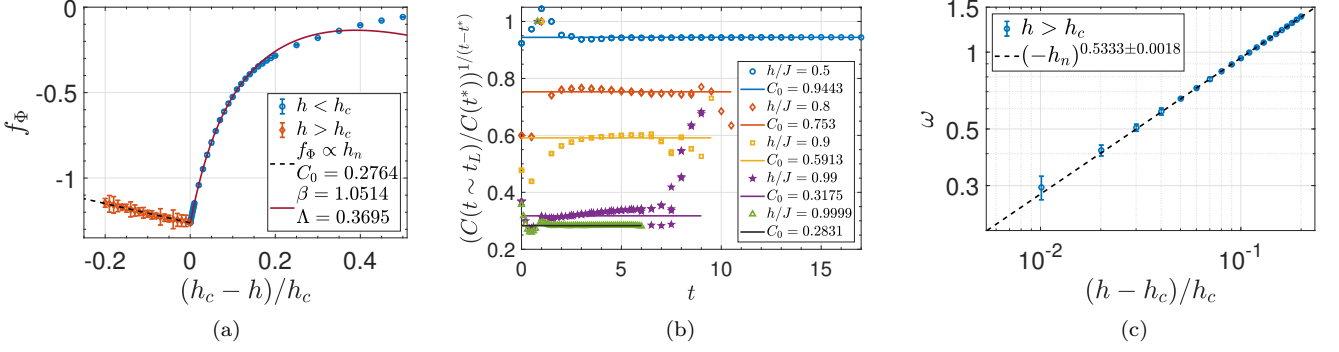


FIG. 3. (a) Decay rates  $f_\Phi$  for integrable TFIM in dynamically-ordered (blue-circles) and -disordered (red-diamonds) phases. The dynamical transition is signaled by a kink structure at  $h_c = 0.9999 \pm 0.0001$ . Solid-red line is the logarithmic model to describe the ordered phase, whereas the black-dashed line is the linear model for disordered phase. (b) Rescaled y-axis is plotted against time for different  $h/J$  (see legend). The solid flat lines are exponential model prediction while the data accumulates around them with slight divergences (see text). (c) Angular frequency scales with  $-h_n$  with a power-law exponent of  $\delta \sim 0.5$  in the disordered phase at the vicinity of the transition.

non-universal short-distance details and finite-size effects are suppressed as detailed above. This intermediate time range whose corresponding spatial region remains in the lightcone is also the transient regime of the dynamics. Thus any dynamical OP constructed in the lightcone should be rescaled correctly with the cutoff time. Fig. 2 shows how the rescaled dynamical OP constructed based on different cutoffs scales with  $h_n = (h_c - h)/h_c$  at the vicinity of the transition. The colors yellow, red and blue correspond to cutoffs chosen at fixed  $t_L = 2.5, 4, 5.5$  (plus markers) and at  $\alpha = 5, 8, 11$  for parametric  $t_L = \alpha/v_q$  (triangle markers). All data accumulate closely to each other and in particular data for different temporal cutoffs collapse perfectly [40]. Such scaling behavior at the vicinity of a dynamic transition could be explained rather simply in terms of the decay properties of the observable. While the observable decays exponentially in the ordered phase, the exponential decay is superposed with oscillations in the disordered phase  $C(t) \sim \exp(f_\Phi t) \cos \omega t$ , clearly differentiating two dynamic phases from each other. Such an observation was made for the XXZ model in Ref. [36] and similarly we observe a kink in the decay rate which could be marked as the DPT point. The phase boundary separates the dynamically-ordered phase (blue-circles) from -disordered phase (red-diamonds) in Fig. 3a. The transition point reads  $h_c = 0.9999 \pm 0.0001$ . The decay rate in the ordered phase can be found as,  $f_\Phi = \log(\gamma h_n^\beta \exp(-h_n/\Lambda) + C_0)$  (red-solid line in Fig. 3a). We note that such a model for the decay rate is intuitive and explains the data in a large interval  $0 < h_n \lesssim 0.5$ , not only at the vicinity of the transition. The constant  $C_0$  points to the observation that the decay rate is never infinite, however the largest at the transition point. Hence the system thermalizes the quickest at its dynamic transition point. Further  $C_0$  is not a free parameter, but fixed by the data itself at the kink. Data follows  $\log(\gamma h_n^\beta + C_0)$

at the vicinity of the transition, while introducing an exponential cutoff [41] to the model lets us describe a bigger region of  $h_n$  as well as providing a definition for ‘vicinity of the transition’,  $h_n \ll \Lambda$ . The model for the decay rate, in turn, reveals the scaling of the dynamical OP at the vicinity of the transition  $h_n \ll \Lambda$  due to the exponential decay of the observable.

$$\begin{aligned} C(t - t^*) &= C(t^*) \exp(f_\Phi(t - t^*)) \\ &= C(t^*) (\gamma h_n^\beta \exp(-h_n/\Lambda) + C_0) t^{-t^*}. \end{aligned} \quad (2)$$

Hence the correct rescaling for the dynamic OP reads,  $(C(t - t^*)/C(t^*))^{1/(t-t^*)} - C_0$ . We also observe that the finite but largest decay rate at the phase boundary,  $C_0$ , causes a finite baseline value for the dynamically-disordered phase. This is a difference from what one would observe in an equilibrium phase transition, where the OP becomes zero in the disordered phase. Since the decay rate can never be infinite for a locally-connected Hamiltonian,  $C_0 \neq 0$ , and thus the OP  $> 0$  in the disordered phase unless  $C_0$  is correctly subtracted from the OP as stated above.

The black-diamond line in Fig. 2 demonstrates the scaling of OP based on the decay rates and it coincides with the data with only small deviation for larger times. This deviation is due to the inaccuracies in the numerics when modeled by an exponential decay and Fig. 3b demonstrates how data could differ from a perfect exponential model which is denoted by the flat lines for some  $h/J$ . Note that the deviation is larger for larger times at the vicinity of the transition and explains why we do not see a perfect collapse in Fig. 2 (see Supplement S-3 for more details). We obtain a linear scaling OP  $\propto h_n^\beta$  where  $\beta = 0.9999$  when only the data at the vicinity of the transition is used (purple-dotted line in Fig. 2). The vicinity of the transition is found by first fitting the power-law scaling with an exponential cutoff,  $h_n \ll \Lambda \sim 0.37$  which

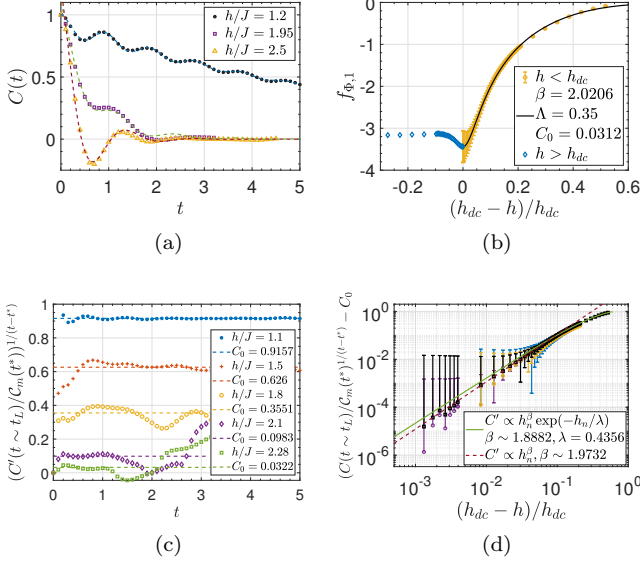


FIG. 4. (a) Nonintegrable TFIM with  $\Delta/J = -1$  for different  $h/J$  values (see legend) and dashed lines are the minimal model predictions for dynamic responses. (b) Decay rate of the first term in minimal model,  $f_{\Phi,1}$  shows a smooth cusp at  $h_{dc} = 2.278 \pm 0.001$  signaling a DPT between the ordered phase (yellow-circles) that can be modeled by logarithmic function (black-solid) and disordered phase (blue-diamonds). (c) Exponential model predictions shown with solid flat lines and rescaled data around them in early times (see text and [40]). (d) Power-law scaling at the vicinity of the transition with an exponent of  $\beta \sim 2$  with blue and yellow data at times  $t = 0.3, 0.5$  and purple data at the nodes of the oscillations (see text).

corresponds to  $h \sim 0.96$  (green-solid line in Fig. 2). The linear scaling is consistent with the kink at the dynamic phase boundary. In the dynamically-disordered phase, the decay rate is linear at the vicinity of the transition,  $f_{\Phi} \propto h_n$  as seen in red-diamonds line of Fig. 3a. Since this phase is oscillatory, we study the angular frequency  $\omega$  and observe that  $\omega \propto (-h_n)^\delta$  where  $\delta \sim 0.5$ , marking  $h_n = 0$  as the transition boundary as well.

*Breaking the integrability.* We break the integrability of the model by taking  $\Delta = -1$  in Eq. 1, which hosts an equilibrium QPT at  $h_c \sim 2.46$  [40]. Fig. 4a shows the sophisticated dynamic response of this model for different  $h$  values in the lightcone determined by data ranging from  $N = 24$  to  $N = 42$ . Lightcone is determined similarly by studying the separation timescales  $\tau_s$  which turns out to be tighter than the timescales predicted by equal-time two-point correlators [40]. An important difference from the integrable model is the oscillations existing in both dynamically-ordered and -disordered phases. Hence we first aim to approximately model the dynamic response. Since oscillations are always present, a minimal model that can reproduce the important features of the dynamics is  $C(t) = \gamma_1 \exp(f_{\Phi,1}t) + \gamma_2 \exp(f_{\Phi,2}t) \cos \omega t$ . The

dashed lines in Fig. 4a show how well the minimal model can describe the dynamics. The first term is the analogous term for the ordered phase of the integrable model, whereas the second term superposes the oscillations with the exponential decay. We focus on the decay rate of the first term,  $f_{\Phi,1}$  since this is the term that governs the exponential decay of the dynamic response (see Supplement S-4 [40]). Fig. 4b demonstrates that a minimum exists for  $f_{\Phi,1}$ , rather different than the kink in integrable model, hence exhibiting a smooth phase boundary for the non-integrable model. We emphasize that this is the boundary where the fastest decay could happen in the model. Thus it is a well-defined candidate for a DPT, following the observations in integrable models. We determine the dynamic phase boundary as  $h_{dc} = 2.278 \pm 0.001$ , which is shifted from the equilibrium transition favoring disorder. The decay rate of the ordered phase follows previously introduced logarithmic scaling in  $h_n$  (Fig. 4b) giving rise Eq. 2 to hold for nonintegrable model, as long as the oscillations are taken care of in the dynamical OP. This could be performed in a couple of different ways, e.g. averaging over a period  $\mathcal{T} = 2\pi/\omega$ , working only at the nodes of the oscillations  $(\pi + 2\pi n)/2\omega$  where  $n \in \mathbb{Z}$  [40] or simply rescaling the dynamic OP accordingly. Another notable difference from the integrable model is that we fix  $t^* = 0.1$  for all  $h/J$  for simplicity of data analysis and rescale the OP with  $\gamma_1$  instead of  $C(t^*)$  (see Supplement S-5 for more details). Fig. 4c demonstrates how well the data can be explained by an exponential decay when OP is correctly rescaled. At the vicinity of the transition, the data coincides well with the flat lines only in early times. This points to the limitations of the minimal model [40]. We plot data taken at  $t = 0.3$  (blue) and  $t = 0.5$  (yellow) in Fig. 4d in addition to data at a node of the oscillation (purple). The black-squares show the dynamic OP derived from the decay rate, Fig. 4b. All data collapses reasonably well and can be described by the power-law scaling of  $\beta \sim 2$  at the vicinity  $h_n \ll \Lambda = 0.44$ , which corresponds to  $h \sim 2.23$ . The scaling exponent is consistent with the smooth transition boundary.

*Discussion.* The exponents derived for the (non-)integrable models are different, hence there is no universality in the sense of equilibrium phase transitions. This is intuitive because the QPT studied here originates from the transient dynamics and cannot be governed only by the ground-state physics (see Supplement S-6 for more details). However the presence of a dynamic scaling law seems to be universal. Interestingly, the dynamic phase boundary coincides with equilibrium counterpart for the integrable TFIM, whereas it shifts to favor disorder for the nonintegrable TFIM. Studying larger system sizes for the nonintegrable models would provide larger time intervals remaining in the lightcone and thus improve the model that describes the data better, which in turn could lead to more precise and accurate predictions on the dynamic phase boundary and the associated scaling law.

Our work opens new avenues to explore non-equilibrium order, with no need for reaching the saturation regime which might be challenging for experiments [29]. There are interesting directions for future, such as (i) the application of the procedure to other short-range Hamiltonians, e.g. the XXZ model; to long-range interacting models with logarithmic lightcones [42]; and 2D Ising models, as well as (ii) determining how the scaling exponent changes with the interaction strength in the TFIM.

*Acknowledgments.* We thank Jad C. Halimeh and L.-M. Duan for helpful suggestions and discussions. DMRG calculations are designed with ITensor [43] and performed by the Great Lakes High Performance Computing Cluster of the University of Michigan. This work was supported by National Science Foundation under Grant EFRI-1741618.

---

\* cbdag@umich.edu

- [1] L. D. Landau, Zh. Eksp. Teor. Fiz. **7**, 19 (1937), [Phys. Z. Sowjetunion **11**, 26 (1937); Ukr. J. Phys. **53**, 25 (2008)].
- [2] J. Zinn-Justin, *Quantum Field Theory and Critical Phenomena; 4th ed.*, Internat. Ser. Mono. Phys. (Clarendon Press, Oxford, 2002).
- [3] S. Sachdev, *Quantum Phase Transitions* (Cambridge University Press, 2001).
- [4] W. H. Zurek, U. Dorner, and P. Zoller, Phys. Rev. Lett. **95**, 105701 (2005).
- [5] B. Damski and W. H. Zurek, Phys. Rev. Lett. **99**, 130402 (2007).
- [6] J. Dziarmaga, Advances in Physics **59**, 1063 (2010).
- [7] A. Polkovnikov, K. Sengupta, A. Silva, and M. Vengalattore, Rev. Mod. Phys. **83**, 863 (2011).
- [8] E. Nicklas, M. Karl, M. Höfer, A. Johnson, W. Muesel, H. Strobel, J. Tomković, T. Gasenzer, and M. K. Oberthaler, Phys. Rev. Lett. **115**, 245301 (2015).
- [9] M. Heyl, A. Polkovnikov, and S. Kehrein, Phys. Rev. Lett. **110**, 135704 (2013).
- [10] M. Heyl, Reports on Progress in Physics **81**, 054001 (2018).
- [11] T. Mori, T. N. Ikeda, E. Kaminishi, and M. Ueda, Journal of Physics B: Atomic, Molecular and Optical Physics **51**, 112001 (2018).
- [12] M. Heyl, F. Pollmann, and B. Dóra, Phys. Rev. Lett. **121**, 016801 (2018).
- [13] C. B. Dag, K. Sun, and L.-M. Duan, Phys. Rev. Lett. **123**, 140602 (2019).
- [14] B.-B. Wei, G. Sun, and M.-J. Hwang, Phys. Rev. B **100**, 195107 (2019).
- [15] M. Eckstein, M. Kollar, and P. Werner, Phys. Rev. Lett. **103**, 056403 (2009).
- [16] B. Sciolia and G. Biroli, Phys. Rev. B **88**, 201110 (2013).
- [17] N. Tsuji, M. Eckstein, and P. Werner, Phys. Rev. Lett. **110**, 136404 (2013).
- [18] J. C. Halimeh, V. Zauner-Stauber, I. P. McCulloch, I. de Vega, U. Schollwöck, and M. Kastner, Phys. Rev. B **95**, 024302 (2017).
- [19] B. Žunković, M. Heyl, M. Knap, and A. Silva, Phys. Rev. Lett. **120**, 130601 (2018).
- [20] J. Zhang, G. Pagano, P. W. Hess, A. Kyprianidis, P. Becker, H. Kaplan, A. V. Gorshkov, Z. X. Gong, and C. Monroe, Nature (London) **551**, 601 (2017), arXiv:1708.01044 [quant-ph].
- [21] P. Titum, J. T. Iosue, J. R. Garrison, A. V. Gorshkov, and Z.-X. Gong, Phys. Rev. Lett. **123**, 115701 (2019).
- [22] J. C. Halimeh and V. Zauner-Stauber, Phys. Rev. B **96**, 134427 (2017).
- [23] F. H. L. Essler, S. Evangelisti, and M. Fagotti, Phys. Rev. Lett. **109**, 247206 (2012).
- [24] P. Calabrese, F. H. L. Essler, and M. Fagotti, Journal of Statistical Mechanics: Theory and Experiment **2012**, P07016 (2012).
- [25] P. Calabrese, F. H. L. Essler, and M. Fagotti, Phys. Rev. Lett. **106**, 227203 (2011).
- [26] M. Gessner, M. Ramm, T. Pruttivarasin, A. Buchleitner, H. P. Breuer, and H. Häfner, Nature Physics **10**, 105 (2014), arXiv:1311.4489 [quant-ph].
- [27] N. A. Sinitsyn and Y. V. Pershin, Reports on Progress in Physics **79**, 106501 (2016).
- [28] B. Neyenhuis, J. Zhang, P. W. Hess, J. Smith, A. C. Lee, P. Richerme, Z.-X. Gong, A. V. Gorshkov, and C. Monroe, Science Advances **3**, e1700672 (2017), arXiv:1608.00681 [quant-ph].
- [29] H.-X. Yang, T. Tian, Y.-B. Yang, L.-Y. Qiu, H.-Y. Liang, A.-J. Chu, C. B. Dag, Y. Xu, Y. Liu, and L.-M. Duan, Phys. Rev. A **100**, 013622 (2019).
- [30] K. Xu, Z.-H. Sun, W. Liu, Y.-R. Zhang, H. Li, H. Dong, W. Ren, P. Zhang, F. Nori, D. Zheng, H. Fan, and H. Wang, arXiv e-prints, arXiv:1912.05150 (2019), arXiv:1912.05150 [quant-ph].
- [31] E. H. Lieb and D. W. Robinson, Communications in Mathematical Physics **28**, 251 (1972).
- [32] P. Calabrese and J. Cardy, Journal of Statistical Mechanics: Theory and Experiment **2005**, P04010 (2005).
- [33] S. Sachdev and A. P. Young, Phys. Rev. Lett. **78**, 2220 (1997).
- [34] P. Calabrese and J. Cardy, Phys. Rev. Lett. **96**, 136801 (2006).
- [35] D. Rossini, A. Silva, G. Mussardo, and G. E. Santoro, Phys. Rev. Lett. **102**, 127204 (2009).
- [36] P. Barmettler, M. Punk, V. Gritsev, E. Demler, and E. Altman, Phys. Rev. Lett. **102**, 130603 (2009).
- [37] A. M. Luchli and C. Kollath, Journal of Statistical Mechanics: Theory and Experiment **2008**, P05018 (2008).
- [38] M. Cheneau, P. Barmettler, D. Poletti, M. Endres, P. Schau, T. Fukuhara, C. Gross, I. Bloch, C. Kollath, and S. Kuhr, Nature **481**, 484487 (2012).
- [39] L. Villa, J. Despres, and L. Sanchez-Palencia, Phys. Rev. A **100**, 063632 (2019).
- [40] See supplementary material.
- [41] A. Clauset, C. R. Shalizi, and M. E. J. Newman, SIAM Review **51**, 661 (2009), <https://doi.org/10.1137/070710111>.
- [42] M. Foss-Feig, Z.-X. Gong, C. W. Clark, and A. V. Gorshkov, Phys. Rev. Lett. **114**, 157201 (2015).
- [43] ITensor Library (version 2.0.11) <http://itensor.org>.

## Supplementary: Quantum phase transitions far from equilibrium in short range transverse field Ising models

In the main text and the supplementary, all data presented belongs to systems quenched from a polarized state.

### LIGHTCONES BASED ON EQUAL-TIME TWO POINT CORRELATORS

In this section, we discuss a well-established way of extracting lightcones applied to our models. One can obtain lighcones and the speed of the correlation spread via the fluctuations of equal-time two-point correlators [S1–S4],  $\langle \delta\sigma_z^r(t)\delta\sigma_z^{r'}(t) \rangle$  where  $\delta\sigma_z^r(t) = \sigma_z^r(t) - \langle \sigma_z^r(t) \rangle$  for pairs of  $(r', r \neq r')$  running from  $t = 0$  to some time  $t$  that reveals the functional form of the lightcone. Then we determine the contours of very small amplitude,  $\xi$  that sets the onset of fluctuations growing  $\langle \delta\sigma_z^r(t)\delta\sigma_z^{r'}(t) \rangle > 0$  for  $t > 0$ . Numerically one can study a set of lightcones with different  $\xi$ . To eliminate this arbitrariness we choose  $\xi$  with the best goodness of fit,  $R^2$  value. We first test this method on integrable TFIM, since its velocity bounds are analytically known.

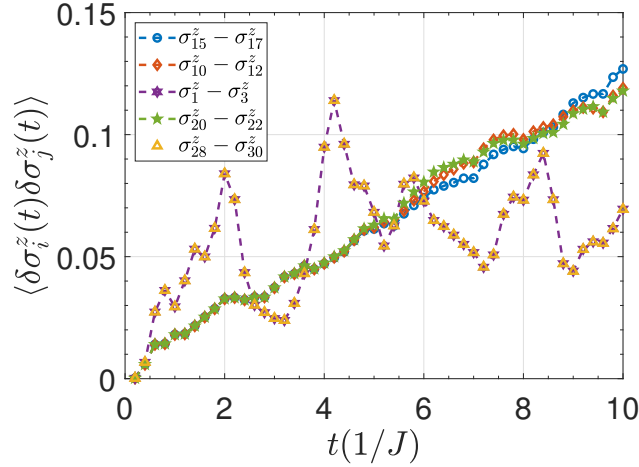


FIG. S1. Two-point correlator  $\langle \delta\sigma_z^r(t)\delta\sigma_z^{r'}(t) \rangle$  for nonintegrable TFIM of system size  $N = 30$ ,  $\Delta/J = -1$  at  $h/J = 0.75$ . The legend shows the pair of initial and final space points  $(r', r \neq r')$  taken all of which has the same distance  $r - r' = 2$ .

While one can choose the initial space coordinate as the first and hence the edge operator of the chain  $r' = 1$  to increase the size of the space dimension as much as possible, we note that this opens a way for the edge effects to appear in the lightcone. To demonstrate how the edge effects might change the lightcone behaviour, we plot Fig. S1 for a system size of  $N = 30$  of nonintegrable TFIM with  $\Delta/J = -1$  at  $h/J = 0.75$ . The plot exhibits  $\langle \delta\sigma_z^r(t)\delta\sigma_z^{r'}(t) \rangle$  for different pairs of  $(r', r \neq r')$  with fixed difference  $r - r' = 2$  stated in the legend. This figure shows taking the reference spin at the edge introduces significant oscillations and completely changes the quantitative behaviour of two-(space)point correlators. Hence for the rest of the study, we set the initial and final points sufficiently away from the edges, e.g. at least  $\sim 10$  units away from the edges.

### Integrable TFIM

Fig. S2 shows lightcones extracted for integrable TFIM of system size  $N = 36$  at different external field values  $h = 0.4, 0.6, 0.8, 0.9$ . Sufficiently away from the phase transition boundary, the best fit reveals the analytically predicted lightcone velocity; while as we approach the boundary, the best fit based on data starts to be smaller than the analytic prediction based on the maximum quasiparticle velocity. We note that the lightcone (or the Lieb-Robinson velocity), is twice the maximum quasiparticle velocity as known in the literature [S1]. Additionally, we find linear lightcones as expected [S2, S3, S5].



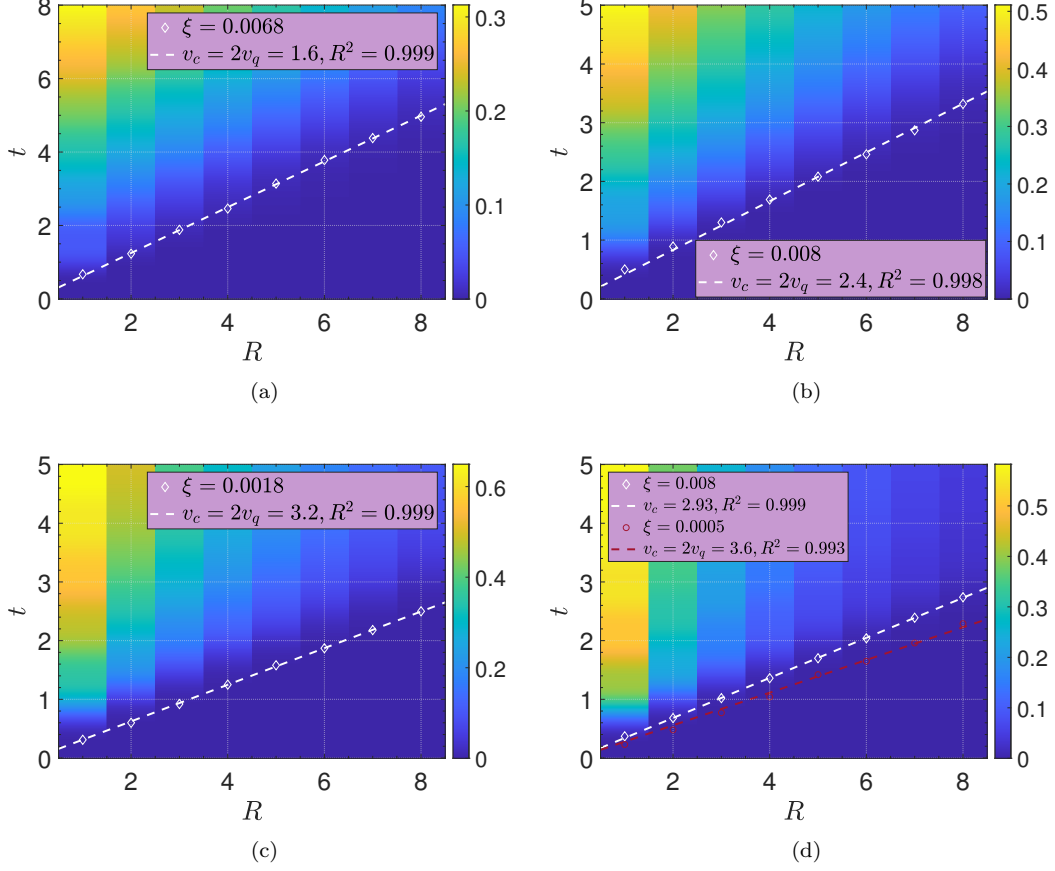


FIG. S2. Lightcones of integrable TFIM at (a)  $h/J = 0.4$ , (b)  $h/J = 0.6$ , (c)  $h/J = 0.8$  and (d)  $h/J = 0.9$  with system size of  $N = 36$  via t-DMRG. In a lightcone figure, x- and y-axes stand for the spatial distance  $R$  and time  $t$ , respectively. The circles are the data points corresponding to the contour threshold  $\xi$  and the fitted dashed lines are the best fits to the data.  $R^2$  in the legend is the correlation coefficient of the fit;  $v$  corresponds to the extracted lightcone velocity at its associated threshold value  $\xi$ . In subfigure (d) the data with white dashed line shows the lightcone with the best fit  $R^2$  value; whereas the red dashed line shows the lightcone agreeing with analytical prediction, even though it is not the best fit.

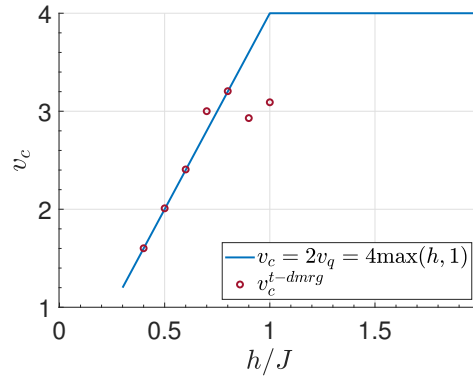


FIG. S3. Lightcone velocity with respect to  $h/J$ . The solid-blue line is analytic, whereas the red-circles show the data from numerics based on  $N = 36$  system size generated via t-DMRG.

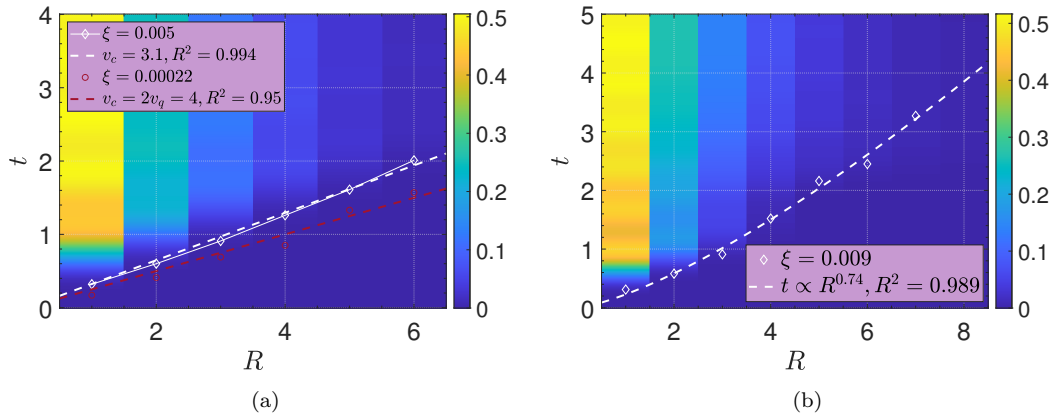


FIG. S4. Lightcones of integrable TFIM at (a)  $h/J = 1$  and (b)  $h/J = 1.2$  with system size of  $N = 36$  via t-DMRG. In subfigure (a) the data with white dashed line shows the lightcone with the best fit  $R^2$  value; whereas the red dashed line shows the lightcone agreeing with analytical prediction, even though it is not the best fit.

We plot the lightcone velocity  $v_c$  with respect to the control parameter, external field values  $h/J$  that originates from analytic prediction (solid-blue) and the data of two-point correlators (red-circles) in Fig. S3. Towards the transition boundary, we observe a difference between analytic prediction and the numerical data computed via t-DMRG for a system size of  $N = 36$ . We note that this is likely to be a finite-size effect, since at the vicinity of the transition the correlation length diverges and finite-size effects become more pronounced in numerics.

Finally before moving on to the nonintegrable TFIM, we note that linearity of the lightcones breaks down as we pass the phase boundary. Fig. S4 shows the lightcone at the QPT  $h/J = 1$  and disordered phase  $h/J = 1.2$ . While at the boundary, the lightcone looks still sufficiently linear, in the disordered phase the lightcones both visually and numerically turn into sublinear form,  $x \propto t^\chi$  where  $\chi < 1$ . As we will show later, this feature is not special to integrable TFIM, instead it also appears in nonintegrable model as well. We emphasize that the form of the lightcone does not affect our results, because the integration of Lieb-Robinson bounds to the DPT definition does not depend on the form of the lightcones. A more practical way of extracting the lightcones based on one-point observables instead of two-point correlators are described in the next section. This latter method is what employ to determine the upper bound of our data in studying the QPT far away from equilibrium.

### Nonintegrable TFIM

In nonintegrable model, we do not have a quasiparticle velocity due to the interactions introduced; hence we work with the lightcone velocity computed from numerics only. Since the nonintegrability is introduced via the NNN terms, the locality of the Hamiltonian is intact in the long distances. Fig. S5 shows lightcones calculated based on two-point correlators at different  $h/J$  values for  $\Delta/J = -1$  TFIM of system size  $N = 36$ . Linear lightcones emerge for sufficiently deep in the ordered phase, providing a well-defined lightcone velocity. The slight divergence from linearity in very small distances is due to the existence of NNN terms, which does not affect the behaviour in long distances (see especially Figs. S5a and S5b). Passed  $h/J = 1.5$ , sublinear lightcones start to describe the data better than linear model (Figs. S5d-S5f). We provide additional evidence for such emergent sublinear cones in TFIM in the next section. Why such transition from linear to sublinear lightcones happens is an interesting question for further studies on nonequilibrium dynamics of clean TFIM systems.

For convenient comparison with the results of the next section, we plot the timescale set by the smallest data size in our data set,  $N = 24$  in Fig. S6. Given the lightcone model and velocities, one can obtain the timescale based on a fixed distance. This fixed distance, taken as  $N = 24$  in Fig. S6, corresponds to distance where the correlations reach to the end of the chain of size  $N = 24$ . Fig. S6 shows the results for both linear and sublinear model. Since sublinear model better explains the data after some  $h/J$  value, we combine both and determine that its scaling with  $h/J$  is roughly linear.



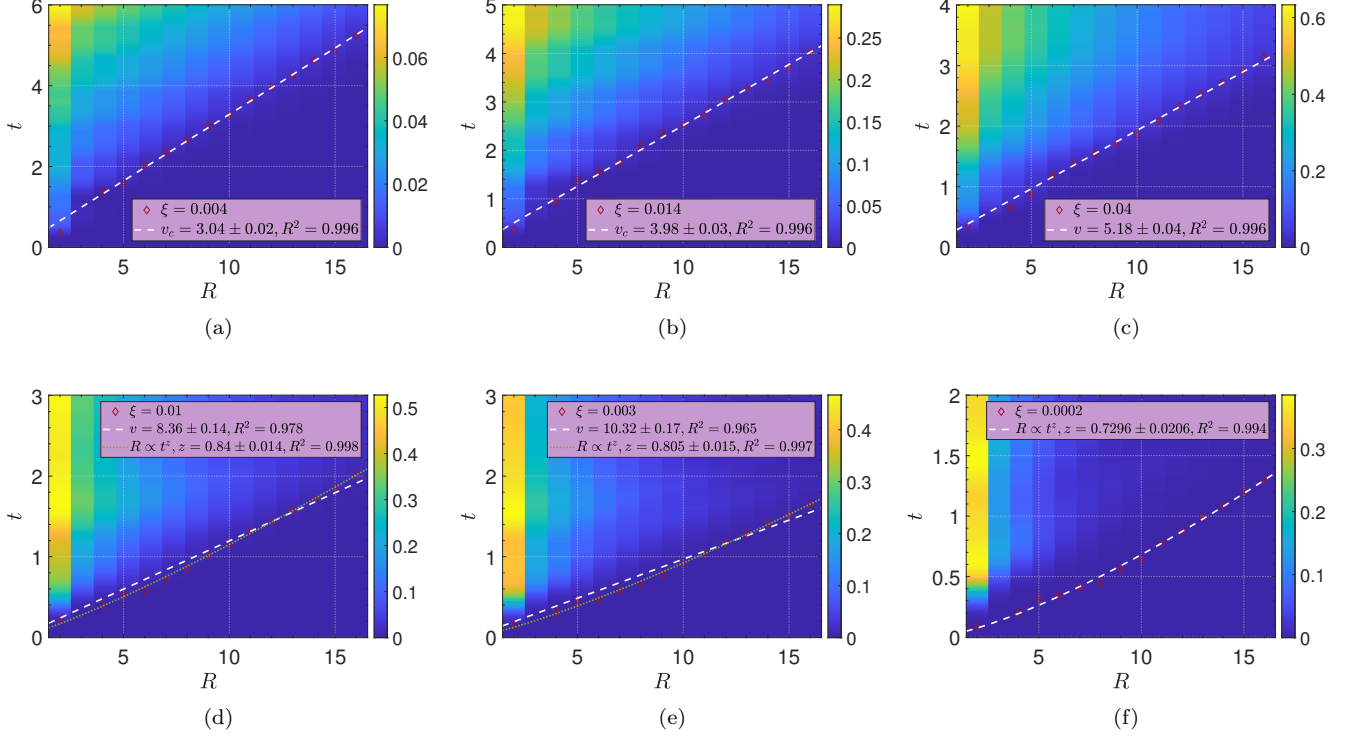


FIG. S5. Lightcones of nonintegrable TFIM with  $\Delta/J = -1$  at (a)  $h/J = 0.75$ , (b)  $h/J = 1$ , (c)  $h/J = 1.4$ , (d)  $h/J = 1.8$ , (e)  $h/J = 2$  and (f)  $h/J = 2.2$  with system size of  $N = 36$  via t-DMRG. In a lightcone figure, x- and y-axes stand for the spatial distance  $R$  and time  $t$ , respectively. The circles are the data points corresponding to the contour threshold  $\xi$  and the fitted dashed lines are the best fits to the data.  $R^2$  in the legend is the correlation coefficient of the fit;  $v$  corresponds to the extracted lightcone velocity at its associated threshold value  $\xi$ . In subfigures (d) and (e), the sets of data are plotted with both sublinear (green dotted) and linear (white dashed) fitting models for convenient comparison.

## EMERGENT LIGHTCONES FROM ONE-POINT OBSERVABLES

In this section, we show that one can extract the lightcones from one-point observables too. We put this method forward as an alternative to the method based on two-point correlators discussed in the previous section. In fact, we (i) explicitly demonstrate that the lightcones generated by one-point observables are tighter in both models and (ii) the method of extracting lightcones based on one-point observables is general to predict forms beyond linear lightcones, e.g. sublinear lightcones emerging in our nonintegrable TFIM.

As we described in the main text, one-point observables of different system sizes can provide us two different but related timescales: separation times  $\tau_s$  and the revival times  $\tau_r$ . Separation time shows when the excitations caused by the quench reach the end of the chain  $\tau_s = N/2v_q = N/v_c$ , whereas the revival time is one round trip of the excitations  $\tau_r = N/v_q = 2N/v_c$  if the initial point is the middle of the chain. We compare  $\tau_s$  timescale with the corresponding timescales derived from the two-point correlators in both integrable and nonintegrable TFIM. In both cases  $\tau_s$  with one-point observables give a tighter bound in time compared to lightcones extracted from two-point correlators. Fig. S7a shows  $\tau_s$  timescale of one-point observables extracted with a resolution of  $\epsilon = 0.005$  (yellow-triangles), which means that we determine  $\tau_s$  when the data for the next system size  $N = 30$  differs from the current system size  $N = 24$  for more than  $\epsilon = 0.005$ . This fixes the time where the data of system size  $N = 24$  starts to experience finite size effects. Yellow-triangles are compared to red-circles which is determined based on the lightcones from two-point correlators. The observation that the timescale predicted by one-point observables is tighter than two-point correlators point out to that in the case of two-point correlators are used to bound the information speed, one-point observables would already have started to exhibit finite-size effects.

In nonintegrable model, the same effect is observed, Fig. S7b where purple-triangles denote  $\tau_s$  for chain size  $N = 24$  and we compare it with the timescale set by the lightcone calculated by two-point correlators, blue-circles. One-point observables provide a tighter timescale, and hence demonstrates that in incorporation of locality (Lieb-Robinson

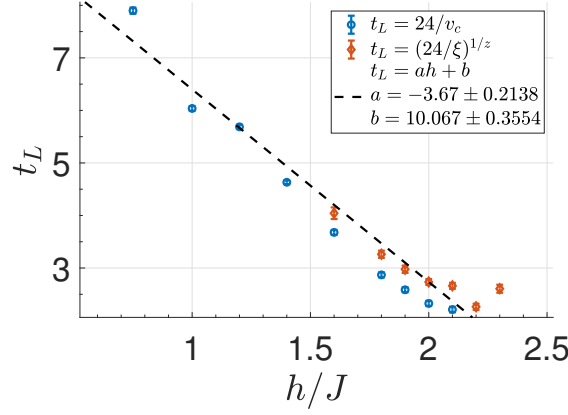


FIG. S6. Timescale  $t_L$  set by the smallest system size in our data set,  $N = 24$  whose explicit form is given in the legend, with respect to  $h/J$ . All computations are done via t-DMRG. Blue-circles are data based on linear model; whereas the red-diamonds are the data based on sublinear model. A linear fit can describe the scaling of  $t_L$  with  $h/J$  in the dynamically ordered phase.

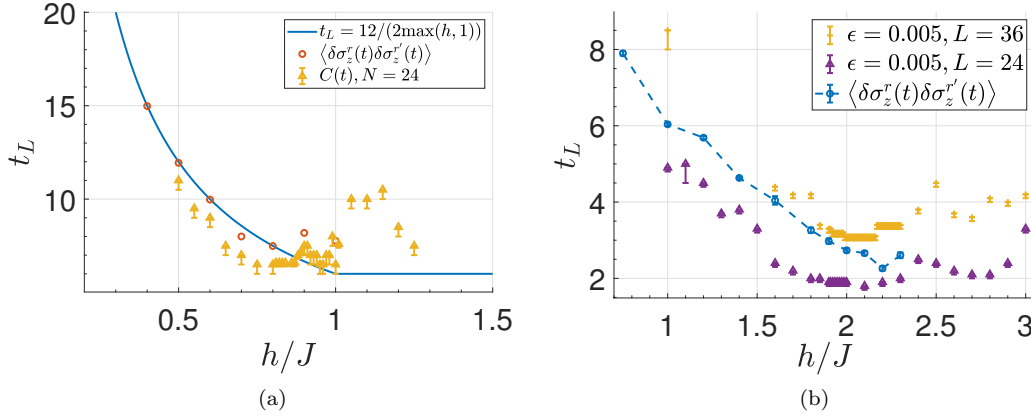


FIG. S7. (a) Timescale set by the smallest chain size in our data set,  $N = 24$  with respect to  $h/J$  for integrable TFIM. Blue solid line is the analytic prediction, red-circles are based on the lightcone velocities extracted from two-point correlators and yellow-triangles are based on the one-point observables. (b) The timescale set by  $N = 24$  (purple-triangles) and  $N = 36$  (yellow-pluses) via one-point observables in nonintegrable TFIM, compared to timescale set by lightcone velocities extracted from two-point correlators (blue-circles).

bounds) into DPT definition, we need to take care of using the timescales set by one-point observables to guarantee remaining in the lightcone. We plotted  $\tau_s$  for  $N = 36$  chain size for reference in Fig. S7b, yellow-pluses. We note that it exhibits the same quantitative trend with  $\tau_s$  for  $N = 24$  (purple-triangles), however in longer time as expected.

To benchmark this alternative method, we set  $h/J = 1.99$  and plot one-point observables of chains with different system sizes in Fig. S8a. Note that even for very large system sizes, the timescale  $\tau_s$  is restricted to early times at the chosen  $h/J$  value. We plot the pairs of  $(R, \tau_s)$  in Fig. S8b for different resolution values ranging between  $\epsilon = 0.001$  and  $\epsilon = 0.005$ . The resulting lightcone is a sublinear lightcone with a dynamical exponent of  $z \sim 0.8$ . This is in perfect agreement with the data from two-point correlators of a very close point,  $h/J = 2$  in Fig. S5e. Note that two differs in the coefficient in front, as expected; because one-point correlators are tighter, their coefficient  $\alpha$  is larger.

## COMPARISON BETWEEN FIXED AND PARAMETRIC TEMPORAL CUTOFFS

In this section, we plot the difference between rescaled OP values with different choices of temporal cutoffs: (i) fixed  $\alpha$  and parametric  $2\alpha/v_q$  (ii) two fixed cutoffs in integrable TFIM. Even though these are clearly distinct temporal cutoffs, the differences are bounded for all  $h/J$  values in the dynamically-ordered phase and more importantly the

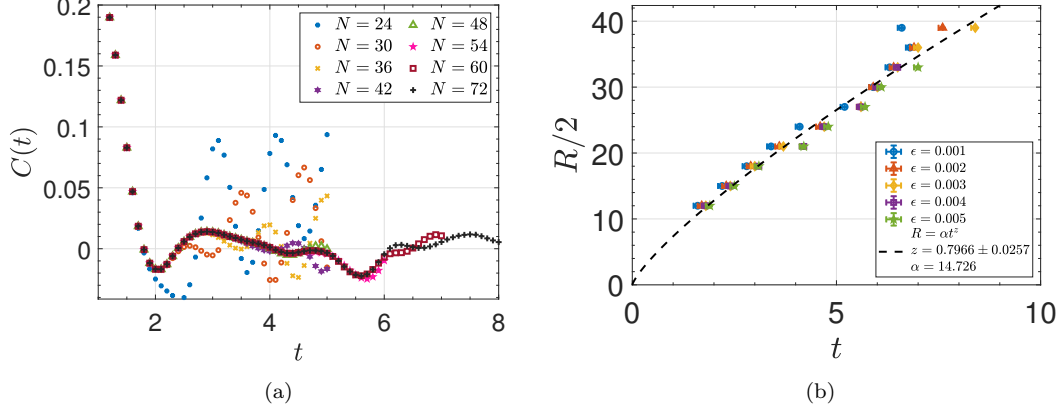


FIG. S8. (a) One-point observable for nonintegrable TFIM  $\Delta/J = -1$  at  $h/J = 1.99$  for different system sizes, see legend. (b) The space-time pairs of  $(R, \tau_s)$  based on separation times plotted to extract the lightcone for different resolutions  $\epsilon$ . The dashed-black line shows the dynamical exponent of the sublinear lightcone discerned from data with  $\alpha$  the coefficient in front, which tells about how tight the lightcone is compared to one extracted from two-point correlators.

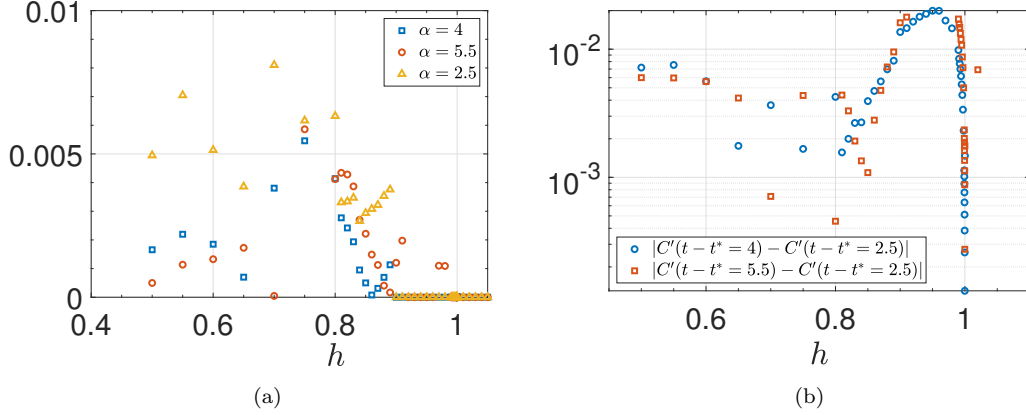


FIG. S9. (a) The differences between rescaled dynamic order parameter of two different temporal cutoffs, parametric  $2\alpha/v_q$  and fixed  $\alpha$  for different  $\alpha$  values (see legend). (b) The differences between rescaled dynamic order parameter of two different fixed temporal cutoffs. See legend.

differences steadily decrease as we approach the phase transition boundary. Fig. S9a demonstrates the differences between rescaled OP values generated with two types of temporal cutoffs for different  $\alpha$  values. They are zero at the vicinity of the transition. This is likely because two types of temporal cutoffs converge to each other as we approach the transition boundary. Fig. S9b shows the differences between rescaled OP values for two fixed temporal cutoffs. In Fig. 2 in the main text, these differences seem to be the largest and we explained the reason based on how well the numerics can model the exponential decay. Here we explicitly plot the differences and show that the differences steadily decrease as we approach the transition boundary.

### MINIMAL MODEL FOR NONINTEGRABLE ISING MODEL

The minimal model for the nonintegrable Ising model reads

$$C(t) = \gamma_1 \exp(f_{\Phi,1}t) + \gamma_2 \exp(f_{\Phi,2}t) \cos \omega t. \quad (\text{S1})$$

We presented how  $f_{\Phi,1}$  scales with  $h_n$  to demonstrate the existence of a smooth dynamic phase boundary in the main text. Here we plot the rest of the parameters with respect to  $h_n$ . Fig. S10 shows, respectively, the coefficients  $\gamma_1$  and  $\gamma_2$ ; the decay rates  $f_{\Phi,1}$  and  $f_{\Phi,2}$ ; and the angular frequency  $\omega$ .

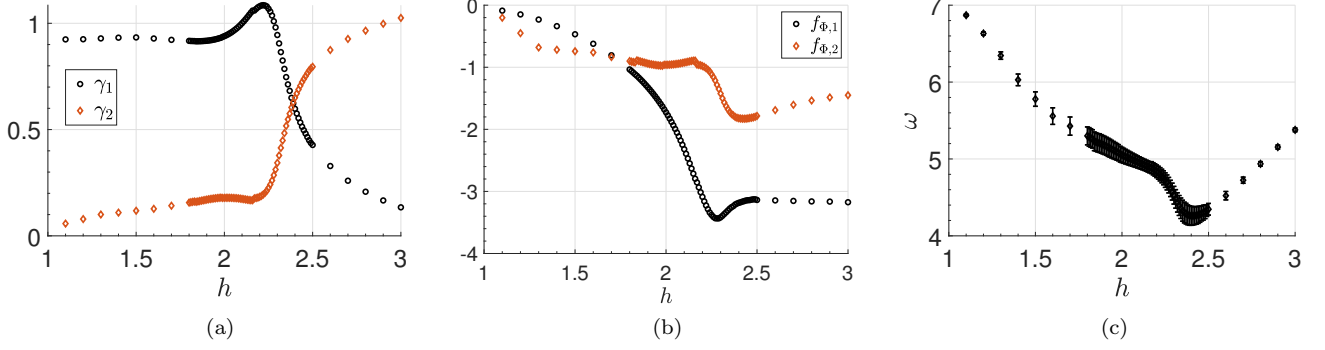


FIG. S10. (a) The coefficients  $\gamma_1$  (black-circles) and  $\gamma_2$  (orange-diamonds); (b) the decay rates  $f_{\Phi,1}$  (black-circles) and  $f_{\Phi,2}$  (orange-diamonds); (c) angular frequency  $\omega$  of minimal model for the dynamics of nonintegrable Ising model.

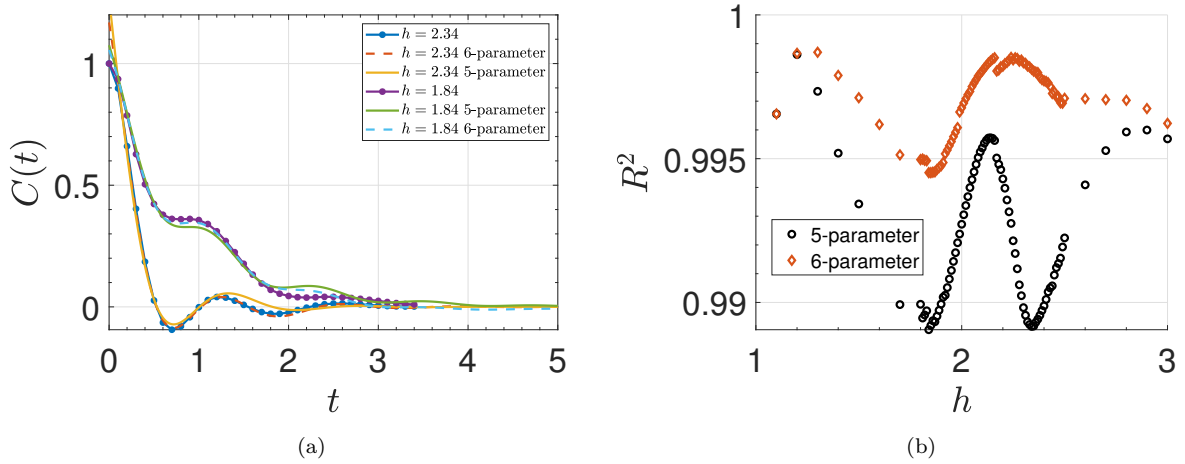


FIG. S11. (a) Dynamic response  $C(t)$  (dotted), minimal (5-parameter) model fitting (solid) and 6-parameter model fitting (dashed). (b) The goodness of fit,  $R^2$  parameter is compared for two models with respect to  $h/J$ .

Based on the coefficients, we observe that the first term is dominant to the second for most of the dynamically-ordered phase; whereas the second (oscillatory) term becomes dominant in the dynamically-disordered phase. This is intuitive given the model and the results of the integrable TFIM. Since the main exponential decay is governed by the first term, we focused on  $f_{\Phi,1}$  in the main text to determine the phase boundary. However both  $f_{\Phi,2}$  and  $\omega$  show extrema features very close to the determined dynamic phase boundary. We do not examine these in detail, since the model could be improved with larger system size data in the future studies to determine features of these parameters with greater accuracy.

We also note that minimal model is likely to work better in early times compared to later times. The reason why we call this model minimal is because there is a 6-parameter model that describes the dynamic response better in details. Namely,

$$C(t) = \gamma_1 \exp(f_{\Phi,1}t) \cos \omega_1 t + \gamma_2 \exp(f_{\Phi,2}t) \cos \omega_2 t. \quad (\text{S2})$$

This model assumes there are two dominant nonzero frequency component in the dynamic response; whereas minimal model studies the limit of  $\omega_1 = 0$ . We emphasize that minimal model is a good approximation especially in the dynamically-ordered phase where  $\omega_1 \ll \omega_2$  is observed from data. It can also capture all important features; while 6-parameter model can predict the details of these features better at the expense of one extra parameter. Fig. S11a shows how two models compare in capturing the dynamic response and Fig. S11b shows their respective  $R^2$  figure of merit, goodness of fit parameter with respect to  $h/J$ . Although for more accurate results, one can model the dynamic response of nonintegrable model with 6-parameter model, we prefer 5-parameter model to minimize the number of parameters as much as possible. Additionally in our 5-parameter minimal model, every parameter is

physically motivated and introducing one more frequency parameter only increases the resolution of the details in the dynamic response. We note that for integrable TFIM, minimal model reduces to one term only where  $\gamma_2 = 0$  in dynamically-ordered phase and  $\gamma_1 = 0$  in the -disordered phase. In this sense, under minimal model integrable and nonintegrable models are quantitatively connected to each other. It is an interesting future study to test the minimal model against nonintegrability strength  $\Delta/J$ .

## DETAILS ON RESCALING THE DYNAMIC ORDER PARAMETER

In this section, we focus on the methods of rescaling the dynamic OP, first in integrable model, later in nonintegrable model.

### Rescaling in integrable TFIM

Rescaling the dynamic OP is a convenient procedure for integrable TFIM due to its simple exponential decay in time. There are two apparent ways of doing the rescaling correctly. The first one uses one free parameter,  $\gamma_1$ ,

$$\left( \frac{C(t \sim t_L)}{\gamma_1} \right)^{1/t_L} - C_0 = h_n^\beta. \quad (S3)$$

However we can get rid of this free parameter, by simply utilizing the data point at reference time  $t^*$  where the exponential decay starts. Hence the rescaling used in the study reads,

$$\left( \frac{C(t \sim t_L)}{C(t^*)} \right)^{1/(t_L - t^*)} - C_0 = h_n^\beta. \quad (S4)$$

We emphasize that  $C_0$  is fixed by data itself at the transition, hence it is not a free parameter.

Here we also answer the question what happens if averaging over a period of time  $T$  is introduced. By a time-averaging integral, the result reads

$$\frac{1}{T} \int_{t_L - T/2}^{t_L + T/2} dt C(t^*) \exp[f_\Phi(t - t^*)] = C(t^*) \exp[f_\Phi(t - t^*)] \frac{\sinh(f_\Phi T/2)}{f_\Phi T/2}. \quad (S5)$$

In the limit of  $T \rightarrow 0$ , we recover the result without averaging. However we note that in case of averaging, one needs to rescale the OP correctly with the averaging interval  $T$  as well in order to reach the dynamic scaling law.

### Rescaling in nonintegrable TFIM

Because two terms exist in minimal model for nonintegrable TFIM, rescaling of the dynamic OP requires attention to get rid of time dependence in the scaling. One of the methods employed in the main text is simple rescaling with subtracting the second term from  $C(t)$ ,

$$C'(t \sim t_L) = C(t \sim t_L) - \gamma_2 \exp(f_{\Phi,2} t_L) \cos(\omega t_L), \quad (S6)$$

hence the rescaling of y-axis reads

$$\left( \frac{C'(t \sim t_L)}{\gamma_1} \right)^{1/t_L} - C_0 = \left( \frac{C(t \sim t_L) - \gamma_2 \exp(f_{\Phi,2} t_L) \cos(\omega t_L)}{\gamma_1} \right)^{t_L} - C_0 = h_n^\beta, \quad (S7)$$

at the vicinity of the transition boundary. However we can find other ways of rescaling the OP to decrease the number of free parameters in the rescaling. In the expression above,  $\gamma_1$ ,  $\gamma_2$ ,  $f_{\Phi,2}$  and  $\omega$  are free parameters.

A quick method to decrease the number of free parameters is to choose  $t_L$  on the nodes of the oscillations. This puts a condition on  $t_L$  as

$$t_L = \frac{\pi + 2\pi n}{2\omega}, \quad n \in \mathbb{Z}. \quad (S8)$$

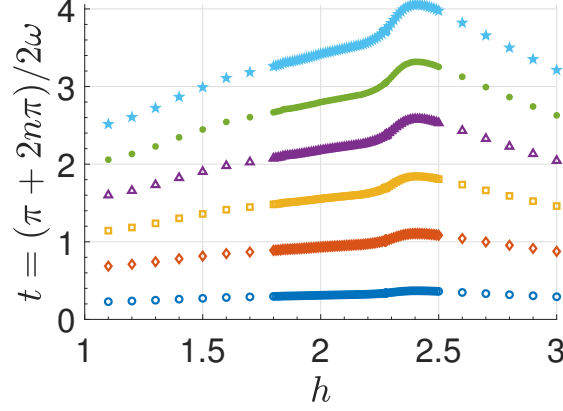


FIG. S12. The condition on the time for the second method described in the text with respect to  $h/J$ . The curves from lowest to highest are denoted by increasing  $n \geq 0$ .

For sufficiently long dynamic response, this condition is not restrictive. See Fig. S12. When the condition is satisfied, the rescaling expression reduces to

$$\left( \frac{C(t \sim t_L)}{\gamma_1} \right)^{1/t_L} - C_0 = h_n^\beta, \quad (\text{S9})$$

with only one free parameter  $\gamma_1$ . This free parameter is hard to get rid of, unlike in integrable TFIM, because oscillations do exist all times and the data for the reference time  $t^*$  is subject to the effect of oscillations too.

Finally one can think of averaging the data as described in the previous subsection. This method requires fine-tuning of  $t_L$  and the averaging interval  $T$  based on the free parameters  $\omega$  and  $f_{\Phi,2}$  to get rid of the second term in minimal model. Even though there happens to be infinite number of possible sets for temporal cutoff and averaging interval  $(t_L, T)$  in total, there are conditions for viable sets  $(t_L, T)$  which brings fine-tuning. Since such a method is likely to be inconvenient both for computation and experiment, we do not discuss it in detail.

### COLLAPSE TIME ANALYSIS FOR SMALL FINITE SIZE SYSTEMS

In this section, we provide further proof of the nonequilibrium nature of the dynamic transition that we have observed and presented in the main text.

Given  $|\psi_0\rangle = \sum_i c_i |\phi_i\rangle$  where  $|\phi_i\rangle$  are eigenstates of the Hamiltonian, a TTC quenched from a polarized state or one-point observable  $C(t) = \langle \psi_0 | \sigma_r^z(t) \sigma_r^z | \psi_0 \rangle = \langle \psi_0 | \sigma_r^z(t) | \psi_0 \rangle$  could be written as,

$$\sum_{ij} c_j^* c_i \langle \phi_j | \sigma_r^z | \phi_i \rangle e^{-it(E_i - E_j)} = \sum_{i \leq j} A_{ij} \cos[\delta_{ij} t]. \quad (\text{S10})$$

Eq. (S10) can be used to estimate a hierarchy of timescales, e.g. quantum collapse and revivals based on the generalization of a method introduced in Ref. [S6]. Here  $A_{ij} = 2c_j^* c_i \langle \phi_j | \sigma_r^z | \phi_i \rangle$  is called overlap distribution and  $\delta_{ij} = E_i - E_j$  is the energy gaps. Estimates for collapse and revivals for a system size of  $N = 14$  are marked by  $\tau_c$  (red-line) and  $\tau_r^{(i)}$  (green lines), respectively, in Fig. S13a that demonstrates a dynamic response at  $h/J = 0.5$  after quenched from a polarized state for integrable TFIM. We observe revivals in effectively infinite time limit  $t \gtrsim N$ , which is consistent with the fact that this is a region where finite-size effects are dominant. Estimated  $\tau_c$  roughly corresponds to a region where the dynamic response reaches its baseline right before finite-size effects kick in. Now let us first discuss how we predict these timescales based on the spectrum properties.

Fig. S13b shows overlap distribution with respect to gaps for  $\Delta = 0$  TFIM with system size of  $N = 14$ . The model under study in Ref. [S6] was a spinor condensate with single mode approximation applied, which simplified the estimations greatly, by focusing only on the first off-diagonal entries of the overlap distribution and the energy gaps [S6]. Here we observe that such a simplification is not possible, because there is not really a pattern of matrix elements that are occupied. Hence we need to generalize this method for irregular distributions like in Fig. S13b and predict a hierarchy of timescales, such as quantum collapse and revivals.



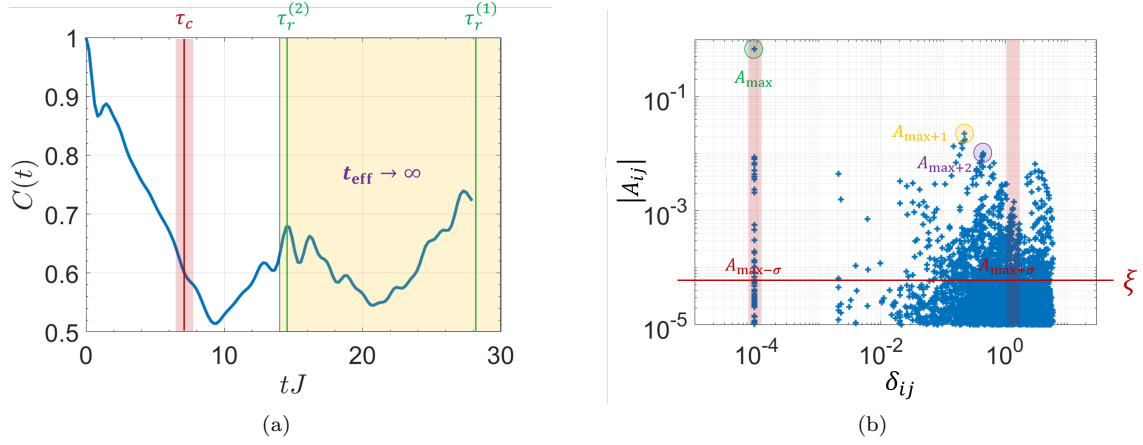


FIG. S13. (a)  $\Delta = 0$  TFIM at  $h/J = 0.5$  at  $N = 14$  exhibits distinct collapse and revival time-scales which we estimate based on spectrum properties. (b) The norm of overlap distribution  $|A_{ij}|$  with respect to energy gaps  $\delta_{ij}$  exhibiting features to estimate distinct timescales of dynamical response. The global and local maxima are circled with green, yellow and purple. The threshold  $\xi$  shows  $1\sigma$  deviation from the maximum of all data, hence helping to determine the collapse timescale (see text). Red translucent boxes show the area to utilize to determine the collapse timescale.

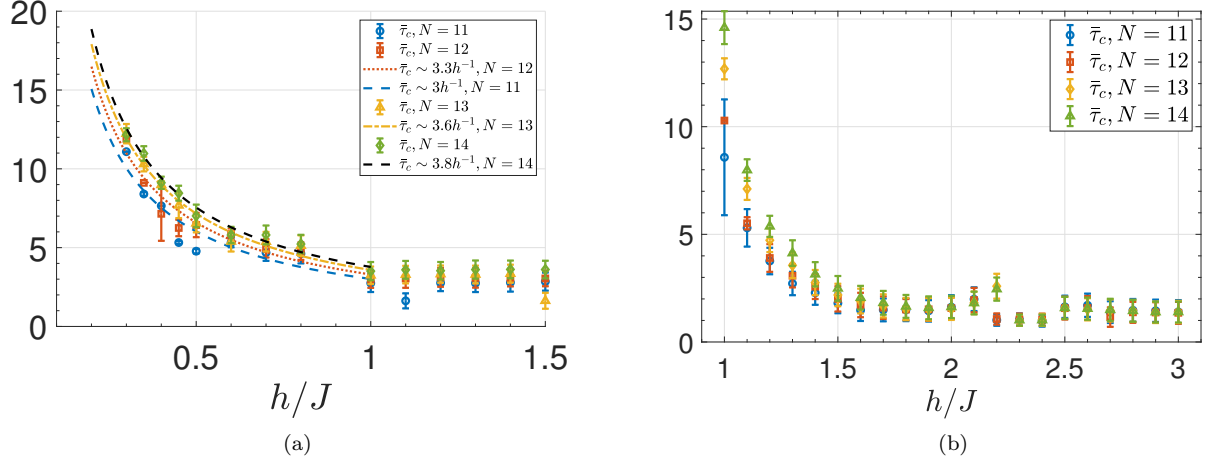


FIG. S14. Estimated collapse timescales for different system sizes ranging between  $N = 11 - 14$  for (a)  $\Delta = 0$  TFIM and (b)  $\Delta = -1$  TFIM. In subfigure (a) the dashed and dotted lines show the fittings of the data to  $\alpha h^{-1}$  which follows the same trend with the lightcone bounds (see legend).

We first reshape the upper (or equivalently lower) triangular part of our overlap  $A_{ij}$  and energy gap  $\delta_{ij}$  matrices into one dimensional arrays with keeping the relation between them intact. This results in Fig. S13b where y-axis stands for the norm of overlap distribution  $|A_{ij}|$  and x-axis for the energy gaps  $\delta_{ij}$ . Even though this does not give a regular distribution, e.g. a Gaussianlike distribution as in Ref. [S6], it still reveals the information necessary to utilize the timescale estimations of quantum collapse and revivals. The analytical estimation for quantum collapse reads,

$$t_c = 2\pi/(\delta_{max+\sigma} - \delta_{max-\sigma}), \quad (\text{S11})$$

where  $max + \sigma$  is  $1\sigma$  standard deviation around the point with maximum amplitude. The reasoning behind this estimation is that finding all relevant data that interferes destructively to give rise to a quantum collapse. We calculate the standard deviation of all data and this provides  $1\sigma$  variation line, which is denoted by the threshold symbol  $\xi$  in Fig. S13b. Any data intersecting with threshold  $\xi$  is a valid data to obtain a collapse timescale. In a regular distribution with a single collapse timescale, there is only one data; however we see that in our overlap distribution we have a set of them. This is not surprising given various oscillatory features in real-time response, which is mostly the finite-size effects, Fig. S13a. At this stage, detecting where the quantum revivals reside in overlap

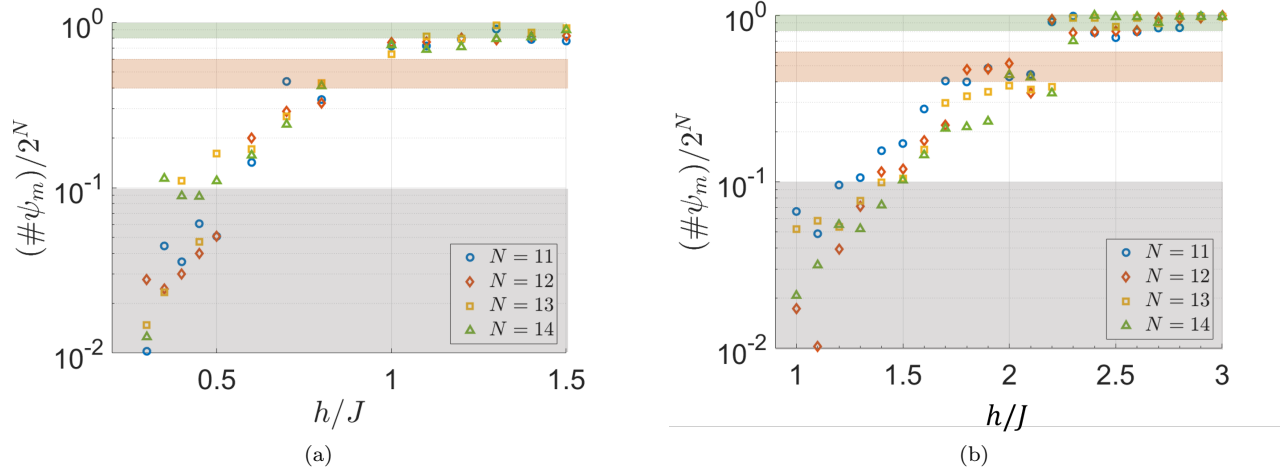


FIG. S15. The excitation ratio,  $\#\psi_m/2^N$ , plotted against the control parameter  $h/J$  for (a)  $\Delta = 0$  and (b)  $\Delta = -1$  TFIM. Grey, red and green boxes correspond to the lowest 0 – 10%, middle 40 – 60% and the highest energy sectors 80 – 100% of the whole spectrum.

distribution is helpful to determine the correct collapse timescale. The analytical estimation for quantum revivals reads,

$$t_r^{(i)} = 2\pi/(\delta_{max} - \delta_{max+i}). \quad (\text{S12})$$

Originally  $i = 1$  only, however we have different local maxima in our overlap distribution, Fig. S13b and hence we could have  $i \geq 1$ . Here  $\delta_{max}$  is the energy gap of the maximum of overlap distribution  $A_{ij}$  and as already mentioned  $\delta_{max+i}$  is the energy gap of the local maxima. We observe three clear local maxima in Fig. S13b which of two are circled with yellow and purple. The highest local minima and vicinity of it (circled with yellow) gives the timescale of the quantum revival marked with  $\tau_r^{(1)}$  on Fig. S13a which is already deep in the effectively infinite time limit and dominated by finite-size effects. The second local minima and its vicinity (circled with purple) gives the timescale of the first ever quantum revival that we mark as  $\tau_r^{(2)}$  on Fig. S13a. Note that this revival also marks the onset of effectively infinite time. Marking these two most obvious quantum revivals in the dynamic response lets us limit our attention to times less than the timescale of the first revival. Times less correspond to energy gaps greater, due to the relation between two, Eq. (S11). Hence we look for the collapse timescale by focusing on the right hand side of the distribution in Fig. S13b. By obtaining a set of fewer and localized times for the quantum collapse, we mark the collapse timescale by averaging this set. The average of the estimated collapse time is marked with red vertical line and the  $1\sigma$  deviation from the mean, with the translucent area around it in Fig. S13a.

We plot collapse times in Figs. S14a-S14b for  $\Delta = 0$  and  $\Delta = -1$  TFIM, respectively. We observe that the collapse times exhibit the same quantitative trend with the lightcone bounds with respect to  $h/J$ . This means that as long as the simulation time remains in the region bounded by the lightcone, the dynamic response experiences quantum collapse. If the chain size is small enough so that the dynamic response cannot fully collapse down to zero as expected from exponential decay, the collapse stops at a baseline value from where one starts to observe quantum revivals as part of finite-size effects. Hence it is plausible to observe that collapse timescale mimics the lightcone bounds dictated by the chain size.

Collapse timescales are contributed by many states. Perhaps this could be more straightforwardly seen in Fig. S13b, given that collapse time-scale is contributed by all states between  $\delta_{max+\sigma}$  and  $\delta_{max-\sigma}$  with an overlap amplitude  $A_{ij} > \xi$ . However we can more explicitly demonstrate this observation by defining a figure of merit. We determine the set of corresponding eigenstates of energy gaps that are found to be relevant in computing the collapse timescales and mark the most energetic excitation as  $\#\psi_m$ . So, the system is capable of having excitations up to the corresponding energy  $E_m$  of eigenstate  $\#\psi_m$ , which results in a quantum collapse. Fig. S15 shows the excitation ratio  $\#\psi_m/2^N$  for both models that reflects how much of the spectrum could be excited after the quench from a polarized state, when the dynamical response is experiencing a quantum collapse. Data for different system sizes exhibit the same trend where  $\#\psi_m/2^N$  steadily increases up until the phase boundary and saturates to  $\#\psi_m/2^N \sim 1$  in the disordered phase, which is the maximum. This means that in the disordered phase the system is able to excite the highest energy levels,

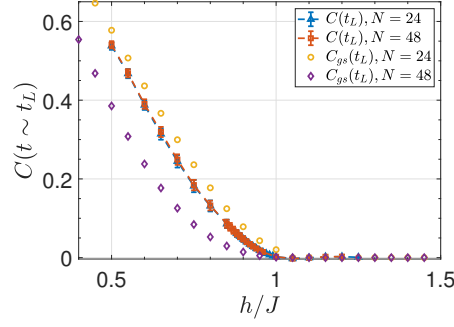


FIG. S16. GS contribution  $C_{gs}(t \sim t_L)$  (DMRG) and the dynamic order parameter  $C(t \sim t_L)$  (t-DMRG) for  $N = 24$  and  $N = 48$  with respect to control parameter  $h/J$ .

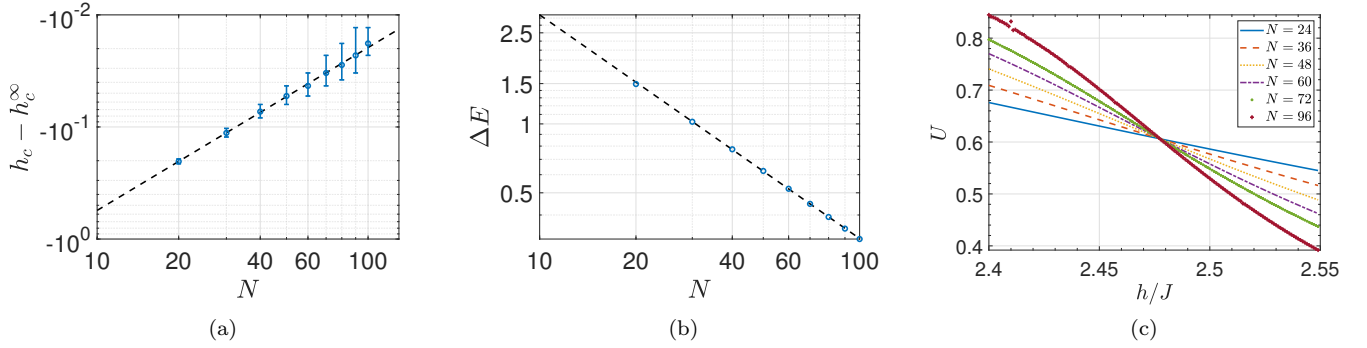


FIG. S17. (a-b) Ground state energy gap analysis with respect to system size  $N$  to determine the equilibrium quantum phase boundary. (a) The critical point is marked as  $h_c^\infty = 2.463$  in thermodynamic limit via scaling analysis. (b) Energy gap  $\Delta E$  closes as we approach the QPT boundary. The scaling exponent is  $\Delta E = N^{-1}$ . (c) Binder cumulant  $U$  for different system sizes ranging between  $N = 24 - 96$ , all crossing at  $h_c = 2.477 \pm 0.001$ .

causing a fast collapse to zero baseline in the dynamic response of the observable. We mark different thresholds on Fig. S15 with translucent boxes; grey, red and green correspond to the lowest 0 – 10%, middle 40 – 60% and the highest energy sectors 80 – 100% of the whole spectrum. Thus, the dynamic order parameter seems to be contributed by states not only in the lowest sector of energy spectrum but also the higher energies as we approach the phase boundary.

A final demonstration of the fact that dynamic order parameter is composed of many nonequilibrium states on top of ground state is plotting the ground state contribution. The GS contribution in the dynamic order parameter reads,

$$C_{gs}(t \sim t_L) = \sum_{i,j=gs} A_{ij} \cos(\delta_{ij}t). \quad (\text{S13})$$

Fig. S16 shows how the ground state contribution  $C_{gs}(t \sim t_L)$  decreases as system size increases, whereas the dynamic order parameter  $C(t \sim t_L)$  is well-defined, meaning that it does not tend to vanish with increasing system size. Even though the dominant contribution in dynamic order parameter is the GS contribution even in moderately large system sizes that we can access via t-DMRG, excitations to higher energy levels due to working in transient regime seem to complement the dynamic order, thus providing a well-defined dynamic phase boundary.

## EQUILIBRIUM QPT BOUNDARY FOR NONINTEGRABLE ISING MODEL

In this section, we present the equilibrium phase transition boundary via both an analysis of ground state energy gap and Binder ratio for the nonintegrable TFIM with  $\Delta/J = -1$ . Figs. S17a-S17b shows the determination of the phase boundary via energy gap analysis. We find that the equilibrium transition happens at  $h_c \sim 2.463$  and the

scaling exponent of the energy gap closing is  $\delta \sim -1$ . Further, we compute the Binder cumulant in Fig. S17c,

$$U = \frac{3}{2} \left( 1 - \frac{1}{3} \frac{\langle S_z^4 \rangle}{\langle S_z^2 \rangle^2} \right), \quad (\text{S14})$$

where  $S_z = \sum_i^N \sigma_i^z$ , the total magnetization operator. This method marks the phase boundary as  $h_c^\infty = 2.477 \pm 0.001$ . The equilibrium transition boundaries determined by these two different methods are very close.

### ERROR BAR CALCULATIONS

The error bars in Figs. 2 and 4d are calculated via error propagation and in Figs. 3a, 3c, 4b they are 1sigma error bars computed via the confidence intervals of the fittings. Given the rescaled dynamical OP is either Eq. (S3) or Eq. (S4), we first see that  $C_0$  is fixed parameter by data in both expressions. In Eq. (S3), there is one free parameter  $\gamma_1$ , which brings an uncertainty of  $\Delta\gamma_1$  that can be computed via the confidence intervals of the fitting. Based on the data points, one can have an uncertainty from  $t_L$  too:  $\Delta t$  denotes this uncertainty which is calculated as the difference between  $t_L$  and the available data point. Hence we can calculate the propagation of error as,

$$E^2 = \left( \frac{\partial \text{OP}}{\partial t} \right)^2 (\Delta t)^2 + \left( \frac{\partial \text{OP}}{\partial \gamma_1} \right)^2 (\Delta \gamma_1)^2, \quad (\text{S15})$$

where OP stands for rescaled dynamic order parameter. Note that if one uses the rescaling for nonintegrable TFIM, additional terms should be added to this expression. The terms in the expression above reads

$$\begin{aligned} \frac{\partial \text{OP}}{\partial \gamma_1} &= -\frac{C(t)^{1/t}}{t} \gamma_1^{-1/t-1}. \\ \frac{\partial \text{OP}}{\partial t} &= -t^{-2} \left( \frac{C(t)}{\gamma_1} \right)^{1/t} \log \left( \frac{C(t)}{\gamma_1} \right). \end{aligned}$$

The error propagation also explains the reason of large error bars in Fig. 4d in main text. These error bars mainly originate from the large error bars of the fitting parameters when we model the dynamic response via minimal model.

---

\* cbdag@umich.edu

- [S1] P. Calabrese and J. Cardy, Phys. Rev. Lett. **96**, 136801 (2006).
- [S2] A. M. Luchli and C. Kollath, Journal of Statistical Mechanics: Theory and Experiment **2008**, P05018 (2008).
- [S3] M. Cheneau, P. Barmettler, D. Poletti, M. Endres, P. Schau, T. Fukuhara, C. Gross, I. Bloch, C. Kollath, and S. Kuhr, Nature **481**, 484487 (2012).
- [S4] L. Villa, J. Despres, and L. Sanchez-Palencia, Phys. Rev. A **100**, 063632 (2019).
- [S5] E. H. Lieb and D. W. Robinson, Communications in Mathematical Physics **28**, 251 (1972).
- [S6] C. B. Dağ, S.-T. Wang, and L.-M. Duan, Phys. Rev. A **97**, 023603 (2018).
- [S7] C. B. Dağ, K. Sun, and L.-M. Duan, Phys. Rev. Lett. **123**, 140602 (2019).